Accessing the third dimension in Localization-based Super-Resolution Microscopy

Journal:	*Physical Chemistry Chemical Physics*
Manuscript ID:	CP-PER-03-2014-001380.R1
Article Type:	Perspective
Date Submitted by the Author:	07-May-2014

Complete List of Authors:	Hajj, Bassam; Institut Curie, Physico Chimie; Janelia farm Research Campus, Transcription Imaging Consortium El Beheiry, Mohamed; Institut Curie, Physico chimie Izeddin, Ignacio; Ecole Normale Supérieure, Institut de Biologie de l'ENS darzacq, Xavier; Ecole Normale Supérieure, Institut de Biologie de l'ENS; Janelia Farm Research Campus, Transcription Imaging Consortium Dahan, Maxime; Institut Curie, Physico chimie; Janelia Farm Research Campus, Transcription Imaging Consortium

PCCP

RSCPublishing

REVIEW ARTICLE

Accessing the Third Dimension in Localization-based Super-Resolution Microscopy

Cite this: DOI: 10.1039/xoxxooooox

Bassam Hajj [a,b,*], Mohamed El Beheiry[a,b,*], Ignacio Izeddin[c], Xavier Darzacq[b,c], Maxime Dahan[a,b]

Received ooth January 2012,
Accepted ooth January 2012

DOI: 10.1039/xoxxooooox

www.rsc.org/

Only a few years after its inception, localization-based super-resolution microscopy has become widely employed in biological studies. Yet, it is primarily used in two-dimensional imaging and accessing the organization of cellular structures at the nanoscale in three dimensions (3D) still poses important challenges. Here, we review optical and computational techniques that enable the 3D localization of individual emitters and the reconstruction of 3D super-resolution images. These techniques are grouped into three main categories: PSF engineering, multiple plane imaging and interferometric approaches. We provide an overview of their technical implementation as well as commentary on their applicability. Finally, we discuss future trends in 3D localization-based super-resolution microscopy.

Introduction

In the past decade, it has become possible for researchers to optically resolve details of biological specimens at the nanoscale. This revolutionary advance was enabled by the class of microscopy techniques that permit imaging below the Abbe diffraction limit,[1] commonly referred to as super-resolution microscopy.[2-9] Super-resolution microscopy techniques are numerous and possess distinct functionality and applicability. In Stimulated Emission Depletion (STED) microscopy, a diffraction-limited excitation focal spot overlaps an engineered donut-shape depletion zone. Fluorescence emission is limited to an area below the diffraction limit, allowing super-resolution information to be obtained through raster-scanning of a sample under study.[10] Structured Illumination Microscopy (SIM) is a wide-field technique in which a sample is illuminated with a grid excitation at different angular orientations, allowing information below the diffraction limit to be unveiled through specialized image processing.[11] This review focuses on a third class of methods referred to as Localization Microscopy (LM), which include Photo-Activation Localization Microscopy (PALM)[12] and Stochastic Optical Reconstruction Microscopy (STORM).[13]

LM takes advantage of the recent development of photo-activatable and photo-switchable fluorescent proteins and dyes. These fluorophores have the characteristic of being stochastically activated upon excitation at a specific wavelength (often in the near UV, around 400 nm).[12-15] Fluorescence emission (readout) occurs upon illumination at a distinct excitation wavelength, in the visible spectrum. Effectively, in any single image of an acquisition sequence, only a sparse number of fluorophores will be activated, allowing them to be individually distinguished. Through numerical fitting (typically with a Gaussian profile), these fluorophores can be localized with high accuracy. The localization accuracy, which depends primarily on the signal-to-noise ratio with which they are detected, is improved by roughly an order of magnitude over the optical diffraction limit. This process of localization is applied on all relevant emitting fluorophores in every image of an acquisition sequence. Super-imposing all localizations eventually forms a super-resolution pointillist picture of the biological specimen under study. The distinction between PALM and STORM lies in the type fluorescent marker that is employed; the former uses fluorescent proteins, the latter uses synthetic dyes. Initially, PALM and STORM techniques were developed for Total Internal Reflection Fluorescence (TIRF) microscopy, where only the basal membrane of a cell is illuminated and imaged.[12, 13] Clearly, many biological specimen of interest have a 3D structure that extends beyond the close proximity (less than ~500 nm) of the cover glass that is accessible with TIRF. There is hence a logical imperative for researchers to record 3D super-resolution images.

Accessing three-dimensional information has long been an important challenge in LM. Inherent difficulties are tied to the wide-field illumination configuration, which is commonly used in LM experiments (**Figure 1**-a). A first issue is the limited depth of field, which typically does not exceed 1 μm in LM experiments. Second, as activation and excitation light illuminate the sample along the optical axis, molecules will be activated throughout the volume of the sample resulting in captured images containing a non-negligible signal component of light emanating from out-of-focus fluorophores. This causes elevated background intensity levels and reduced signal-to-noise ratios for the detection of pertinent in-focus

fluorophores. Furthermore, out-of-focus fluorophores can also be bleached, causing a loss of potential information over the course of an acquisition.

Recent approaches have been proposed to account for the challenges presented with super-resolution 3D LM. To this end, 3D LM techniques can be broadly classified in three categories: PSF engineering, multiple plane imaging, and interferometric approaches. In this review, we describe 3D LM methods pertaining to these categories and, importantly, we highlight their applicability in the context of biological imaging. Although we primarily discuss microscopy tools for 3D super-resolution imaging, it is noted that many of the techniques we shall discuss can and have been applied for 3D single particle tracking (SPT), which itself is an active field in cellular biology and biophysics.[16]

3D Imaging Techniques

The distribution of light originating from a point emitter (in the case of LM, an individual photoactivated fluorophore) is embodied by the point-spread function (PSF) of the imaging system. In an aberration-corrected wide-field microscope, it is most often approximated to have an isotropic Gaussian profile in the lateral (x, y) dimensions (**Figure 1**-b), whose full-width-at-half-maximum (FWHM) is equal to:[17]

$$FWHM_{x,y} = \frac{\lambda}{2NA} \quad (1)$$

where λ is the emission wavelength and NA is the numerical aperture of the microscope objective. In contrast, the FWHM of the PSF in the axial (z) dimension is expressed as:

$$FWHM_z = \frac{2\lambda}{NA^2} \quad (2)$$

In single molecule experiments, high NA objectives are used to collect as many photons as possible. Physical limitations restrain the maximum collection NA to about 1.45 for oil immersion objectives. In this case the extent of the axial profile of the PSF can typically approach ~750 nm, roughly 2.5x that of the lateral profile (**Figure 1**-b).

Imaging systems that use pixelated detector arrays (e.g. EMCCD cameras) capture discretized lateral intensity distributions of the PSF, from which 3D localization of the emitter should be inferred. The distribution of the light intensity on the camera can be fitted to an adequate model, allowing for a lateral localization of the single emitter with a precision limited by the number of detected photons and influenced by pixelation effects.[18, 19] In contrast, axial position is not as readily discernible. This is due to two main reasons. First, in the absence of aberrations in the optical system, the PSF shape is symmetric around the optical axis and the focal plane. Second, the lateral width of the PSF varies only slowly near the focal plane (before rapidly expanding further away).

An early approach for determining the axial location of a point emitter involved measuring the shape of the cross-sectional profile of the PSF in an off-focus imaging scheme and correlating it to a depth position.[20] Although probing depths upwards of 3 µm were achievable with sub-nanometer localization precision, it was limited to observing bright fluorescent beads. Fluorescing species in PALM and STORM experiments are not nearly as bright, making determination of their axial positions based solely on cross-sectional PSF widths a challenging and impractical undertaking.

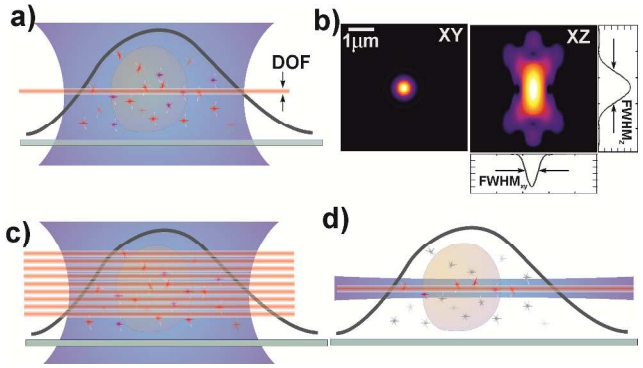

Figure 1: a) In the conventional wide-field imaging configuration, only the volume inside the depth of field (DOF) corresponding to the microscope objective is imaged. The out-of-focus emitting molecules contribute to the background of the recorded images. b) The point spread function (PSF) of a typical wide-field microscope shown by the lateral and axial cross-sections, the latter being in log scale. The profile of the PSF is shown in linear scale. This PSF is a simulation for an aberration-free imaging system using a 1.4 NA objective lens. c) The multifocus imaging modality, simultaneously images multiple planes to cover a larger volume in comparison to conventional wide-field imaging. d) The selective plane illumination configuration, which is used to reduce out-of-focus emission.

The difficulties in the 3D localization of individual emitters in a wide-field microscope can be overcome when certain adjustments are accommodated in the imaging system. The main approaches regroup in the following: breaking the symmetry of the PSF by introducing a controlled aberration in the optical system to engineer the PSF shape, sampling the PSF on multiple focal planes, and increasing the solid angle of photon collection using two opposing objectives combined with interference for enhanced localization precision. We detail the principle of each of these methods whose performance are summarized in **Table** 1.

PSF Engineering

A direct approach to localize individual emitters in 3D consists in engineering the shape of the PSF in order to break its axial symmetry, and such that the form of the PSF lateral cross-section corresponds to a certain depth of the emitter with respect to the focal plane. A calibration curve or lookup table describes this relationship. Among the techniques for engineering the PSF are the astigmatism and double-helix methods, as well as the recently introduced self-bending PSF.

Astigmatism. A popular method that elucidates information on the axial position of an emitter is the imposition of astigmatism in the microscope emission path.[21] A cost-effective solution is realizable by adding a weak cylindrical lens (typically with a nominal focal length of ~ 10 m) in the infinity part of the microscope.[21, 22] We have also reported a more involved approach that consists of using adaptive optics with a deformable mirror, which provides the advantages of tunable astigmatism levels and aberration-correction.[23] Astigmatism has the effect of axially separating the x and y focal planes, such that the ellipticity of the PSF becomes dependent on its z

position. As shown in **Figure 2**-a, the PSF is symmetric at the focal plane, and elongates in either x or y as a function of negative or positive defocus. Fluorophore detections from an image sequence are typically fitted by an asymmetric Gaussian profile which enables retrieval of the widths of the PSF in x and y. These widths serve as input to a calibration curve, which gives a corresponding axial position. In part due to its straightforward implementation and low-cost, astigmatism-based techniques of 3D LM have been widely used. For instance, it has been employed to image actin cytoskeleton,[24] neuronal synapses,[25] and synthetic polymer chains.[26]

Table 1 : Summary of the differences in performance of 3D super-resolution localization microscopy techniques

Imaging Modality		Probe Depth [μm]	Lateral Precision [nm]	Axial Precision [nm]	Live Cell Reported	Multi-Channel Reported	ref
PSF Engineering	Astigmatism	0.75	20	50	Yes	Yes	[22, 23]
	Double-Helix	1.5–2.0	20	50	Yes	Yes	[27, 28]
	SB-PSF	3	10-15	10-15	No	No	[29]
Multi-Plane	Biplane	1	30	75	Yes	Yes	[30, 31]
	MFM	4	20	50	Yes	Yes	[32]
Interferometric	iPALM	0.225-0.750	15	10	No	No	[33-36]
	4Pi SMS	0.650	8.3-22	5.4-6.6	Yes	Yes	[37]
Other Methods	VVSRM	0.750	20-100	20-100	No	No	[38]

A significant challenge with astigmatism-based techniques is the strong sensitivity in *z* localization precision on distortion strength, defocus distance, and detection localization algorithm (in addition to photon counts). Different magnitudes of astigmatic distortion have been shown to adversely affect the *z* localization precision.[23] A high sensitivity in lateral PSF shape (*x* and *y* width) with the relative *z* position ensures an accurate depth localization precision. However, the greater the magnitude of the lateral distortion, the more the PSF spreads, resulting in an overall weaker emitted signal. Effectively, this highlights a tradeoff between the magnitude of the astigmatism and signal-to-noise ratio. In practice, a strong distortion for reasonably bright fluorophores will ensure an axial localization precision of roughly 50 nm or less, with probing depths of approximately 750 nm. Recently, it was shown that a dual-objective approach can provide a marked improvement in photon counts, enhancing *z* localization precision by a potential factor of 1.4.[24]

The contribution of out-of-focus light due to the wide-field excitation configuration can be addressed using light-sheet microscopy. By using a thin sheet of light to excite the sample or to activate molecules, only emitting molecules located in a specific plane contribute to the captured image (Figure 1-d). Light sheets typically range from 1–2 μm thickness,[39] closely corresponding to the conventional wide-field focal depth of ~1 μm. For 3D localization of emitters within the light sheet, the PSF must have axial information encoded, justifying its use with astigmatism to achieve sub-diffraction imaging.[39] Light sheet microscopy has been successfully demonstrated by focusing an excitation beam with a cylindrical lens on live cells [39] and through the use of selective-plane two-photon activation with temporal focusing.[40, 41] The latter approach was demonstrated to achieve whole-cell super-resolution imaging when combined with axial scanning focusing.[40, 41]

Double-Helix PSF. Depth information of an emitting single particle can be encoded in the PSF when it takes the form of a double-helix in the axial direction (**Figure 2**-b).[27] By introducing a spatial light modulator (SLM) loaded with a double-helix PSF (DH-PSF) phase mask in the Fourier plane of the objective of a wide-field microscope, the lateral cross-section of the PSF decomposes into two dominant lobes, as in an idealized double-helix. Effectively, the two lobes rotate about each other as the axial position is changed. Accordingly, the angle between the two lobes gives an estimate of the axial position of the emitting molecule. Lobes are fitted either with a least-squares Gaussian or centroid fit, whereupon the angle between the lobes is determined. As with the astigmatism-based technique, a calibration curve is constructed a priori to correlate the angle between the lobes and the PSF axial position.

The DH-PSF method has been used for multicolor imaging of live bacterial protein ultrastructures where lateral and axial localization precisions of 25 nm and 50 nm have been reported, respectively, along with a probing depth of ~1.5 μm.[28] The DH-PSF method may encounter challenges in densely emitting biological samples, where lobes may overlap, rendering single-molecule discrimination difficult. Furthermore, the SLM is polarization-sensitive and incurs a heavy photon loss (upwards of ~60%) that may limit its use to very bright fluorophores and impose constraints related to fluorophore switching rates to account for lengthier exposure times. Recently, surface-relief phase masks have been used to compensate these effects for the DH-PSF, where photon collection efficiencies may reach 90%.[42]

Another method in which axial position is determined via angular deviations of PSF features, is the corkscrew PSF, which has yet to be reported for super-resolution imaging. In this case the PSF is made to have a lateral elliptical cross-section that rotates as a function of the emitter axial position.[43]

Self-Bending PSF. A recently presented technique involves engineering the PSF such that it takes the form of an Airy beam, which has notable limited diffractive characteristics.[29] It involves splitting the emission channel into two paths, where each respective wave front is modulated with an SLM that, in turn, models the PSF into two self-bending Airy beams. The two images are then projected side-by-side on a single camera detector. A single emitter within the axial detection range is seen as a point in each of the images, where the relative distance between the two defines the final axial position. An

isotropic localization precision of ~10-15nm is obtained using this method over a 3 μm axial range, albeit with ~2000 photons per emitter.

Multiplane Approaches

Biplane. As discussed, the PSF cross-section width slowly varies near the focal plane, making it difficult to determine the z-position solely from a single 2D PSF fit. This difficulty can be overcome by recording two images of the same emitter, taken at different focal positions. The emission pathway may be split into two separate paths, where the light is captured by two cameras conjugated with two different planes of the sample (**Figure 2**-c). The vertical separation of the two planes is usually between 500 nm and 1 μm, such that an emitter will always be out-of-focus on at least one of the cameras. Known as the biplane configuration, the simultaneous projection of the PSF shape on two different cameras can be used to infer the axial position of the emitter.[44] The depth over which objects can be localized varies according to the signal strength. It has been reported to be ~ 1 μm for fluorescent proteins and dyes and ~ 2 μm for brighter probes such as quantum dots and beads.[45]

The first implementation of the biplane technique for LM super-resolution imaging was reported for the study of fluorescent molecules on the surface of 4 μm diameter beads.[31] In this case, sequential *z*-scanning was employed to cover the entire axial extent of the bead. It has been recently used for super-resolution imaging of mitochondria networks,[46] tubulin fibers and septin structures.[47] It is noted that the biplane approach can have better performance than PSF engineering techniques,[31] which are prone to PSF aberrations. An inherent advantage of the biplane technique is that 3D localization accuracy is considered uniform over observed volumes,[48, 49] which cannot be claimed about astigmatism methods where the resolution deteriorates far from the focal plane.[30]

Biplane imaging is also a powerful method for 3D single-particle tracking in live cells, as it offers fast acquisition speeds and the flexibility for combination with other excitation or tracking methods.[44, 50, 51] A recent extension of the technique has been shown in which four planes are simultaneously imaged with four different cameras, allowing tracking of bright quantum dots over depths of 8 μm.[51] Dual-objective configurations have also been used with this method, to help mitigate the division of photon counts between multiple detectors.[52]

Multifocus Microscopy. We have recently introduced an extension of the multiplane imaging concept with the development of multifocus microscopy (MFM).[53] MFM is based on the presence of a chirp-distorted diffraction grating placed in the Fourier plane of a wide-field microscope. Emitted light is diffracted into nine central orders, which, after chromatic correction, are separately imaged on a single camera detector. Precise definition and design of the grating distortion ensures that the nine images correspond to nine focal planes equally separated in the specimen being imaged (Figure 2-d). A multifocus microscope is capable of probing a volume of nearly 20×20×4 μm^3 in a single camera exposure, with a recording speed limited only by the camera readout rate (Figure 1-c).

MFM reaches single-molecule sensitivity, making it compatible with PALM and STORM.[32] The recorded PSF can be fitted with a 3D Gaussian fitting algorithm to infer the three dimensional localization of the emitter. Among its reported applications, MFM has allowed whole-cell multicolor super-resolution imaging of yeast cells and organelles in mammalian cells,[32, 54] as well as 3D tracking of individually labeled proteins in the nucleus.[53] A potential limitation to MFM is the combined effect of dividing photons to nine different diffractive orders and the ~65% efficiency with which light is diffracted into the nine central orders. In practice, however, the 3D localization of a PSF sampled on multiple focal planes enhances the lateral localization accuracy, making it comparable to other 3D LM methods.[32]

Interferometric Approach

In localization-based super-resolution microscopy, axial precision can be improved by the self-interference of an emitted wave emanating from a single molecule near the common focus of two collection objectives. This has the added benefit of collecting nearly twice the number of photons from each emitter, as compared to a single-objective setup. The configuration of the optical system can be tuned to allow interference over a wide range of lateral emitter positions to form interference image on the CCD camera for rapid parallel acquisition. Due to the periodic nature of the interference signal, configurations using three or four channels of interference signals are employed.

iPALM (interferometric PALM). iPALM employs a three-way beam splitter configuration, where self-interfered light is recorded on three cameras with amplitudes oscillating 120° out-of-phase.[35] An emitter is detected on the three detectors with three respective intensities. The lateral position can be directly deduced from the captured images by averaging the respective localizations, while the axial position is determined from the relative intensities from the three cameras (**Figure 2**-e).

The significant advantage of iPALM is its near spatially isotropic 3D localization precision. It has a typical precision of 20 nm laterally and 10 nm axially, which surpasses all other 3D super-resolution LM techniques. An inherent limitation to iPALM, however, is depth of focus, which is limited to 225 nm. To improve the axial extent of this method, iPALM has been combined with astigmatic detection to yield a probing depth of 750 nm. As a consequence, the challenges related to astigmatism are encountered, such as deterioration of localization precision near the edges of the recorded volume.

iPALM is particularly useful in biological contexts where thin structures are imaged. For example, it has been used to reveal that that integrins and actin are vertically separated by a ~40 nm core region consisting of multiple protein-specific layers.[33] Efforts to correlate iPALM super-resolution images with electron microscopy have also been recently reported.[34, 36]

4Pi SMS Microscopy (Stochastic mode or Single Marker Switching). The 4Pi method was first proposed for super-resolution single-molecule detection using a four-way beam splitter configuration.[55] A later implementation was referred to as 4Pi-single marker switching (4Pi-SMS).[37] This technique relies on the interference between orthogonal polarizations of photons collected by both objectives. The signals are then tiled on different quadrants of the same CCD detector. 4Pi SMS is able to localize emitting molecules within 650 nm (1.5 times the wavelength). To overcome the ambiguity over the z localization and extend the range of axial positions beyond $\boldsymbol{\lambda/2}$, this technique calculates the phase not only of the Gaussian-weighted intensity of the emission spot but also of its Gaussian-weighted third central moment. 4Pi-SMS has been used to visualize human platelets and tubulin fibers in mammalian cells.[55]

PCCP

RSCPublishing

REVIEW ARTICLE

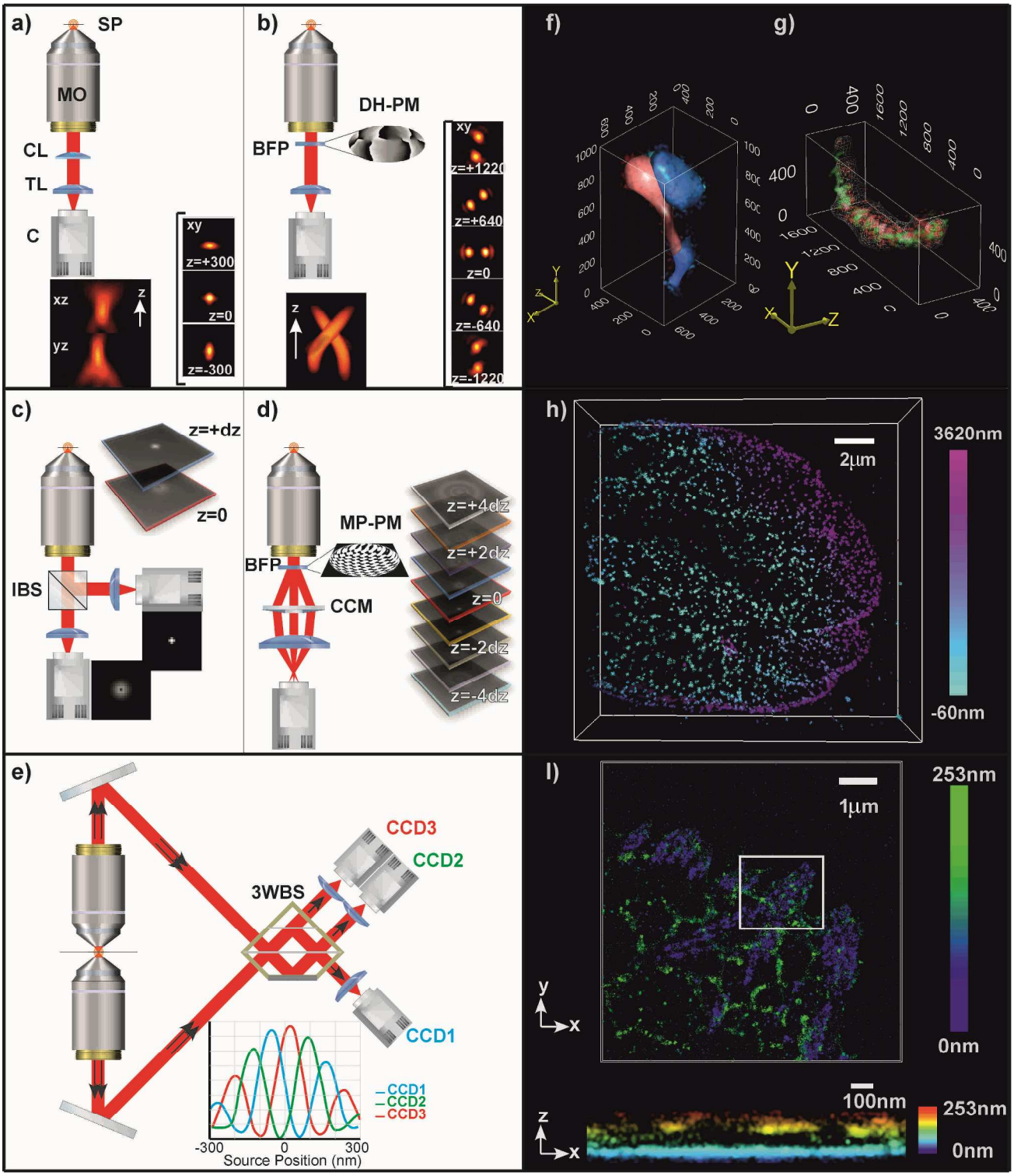

Figure 2 : The different imaging modalities developed for 3D super-resolution imaging. They are divided into three main groups: a-b) PSF engineering c-d) Multiple plane imaging and e) interferometric approaches. a) The astigmatic-based 3D imaging setup, where a cylindrical lens (CL) is placed in the infinity space between the microscope objective (MO) and the tube lens (TL). The image of the PSF shown on the camera (C) is elliptical. The shape defines the position of the emitter along the optical axis. b) The double helix PSF imaging modality, where an adequate phase mask (in reflection or transmission configuration) is placed at the back focal plane of the objective (BFP), inducing a double helix PSF. The two lobs rotate depending on the axial position of the emitter. c) The biplane imaging setup: an intensity beam splitter (IBS) separates the emission into two, the detectors are placed such that they image two different focal planes at the specimen level. The PSF is thus sampled on two different focal planes, enabling a precise localization of the emitter position on the axial axis. d) The multifocus microscopy scheme: a phase mask, placed at the BFP of the objective, splits the emission into nine central orders which are corrected for chromatic aberration using a chromatic correction module (CCM) before being imaged on the camera. The different diffraction orders are corrected for different defocusing power enabling a thorough sampling of the PSF in three dimensions, thus a precise localization along the optical axis. e) The interferometric imaging approach illustrated by iPALM configuration. A three-way beam splitter (3WBS) is used to interfere the light collected by the two objectives. The signal recorded on three cameras is later compared to a calibration signal to recover the axial z position of the emitter. f) An adapted image of the neuronal synapse from ref [25], with the red and blue channels corresponding to gephyrin scaffold proteins expressing mEos2 and glycine receptors tagged with Alexa 647, respectively. g) Multicolor image of a live Caulobacter crescentus bacterium adapted from ref [28] in a colocalization study of the CreS protein h) Depth color-coded super-resolution image of nuclear pore protein POM121 of U2OS cells obtained using the multifocus microscopy for which ~ 3600nm depth was directly reconstructed.[32] i) z color-coded iPALM image of U2OS cells expressing td-EosFP-α_V-integrin. Adapted from Ref [35].

Other Methods

Other methods have been demonstrated for the 3D localization of individual fluorophores, although less common than the ones mentioned above. Virtual Volume Super-Resolution Microscopy (VVSRM) uses a tilted mirror near the objective to create a virtual side-view image.[38] This defocused virtual image is visualized simultaneously beside the real (front) image at the detector by dividing the emission into two using a beam splitter (as is done with the biplane). By combining the front and side view, it is possible to reach a nearly isotropic resolution of better than 100 nm in all directions.[38]

Methods developed in the context of single molecule 3D tracking can likely be extended to super-resolution imaging. The parallax method splits the emission of each fluorophore in the Fourier space into two paths with a sharp edge mirror.[56] The emission is then imaged on two different parts of the camera. Under this optical configuration, a lateral displacement of the fluorophore appears as a shift of the two images in the same direction, while an axial movement will manifest as the images moving toward or away from each other. This method showed good potential in single-molecule tracking over large extent reaching 1 µm, however it suffers from a reduced lateral accuracy (< 200 nm).

Localization Algorithms

Numerically localizing the position of stochastically emitting fluorophores in captured microscopy images is a non-trivial task that has garnered significant attention. The procedure of searching an individual image for fluorescence emission events is typically decomposed into two steps: first, the emission event is identified, and second, the PSF of the emission is fitted to a numerical model. Emission events are usually identified by an intensity local maxima search after a specific image filter has been applied to the image to suppress the appearance of false-positive events due to noise (such as a difference-of-Gaussians filter).

Once the spatial coordinates of the emission event have been determined, the intensity distribution from the emission (i.e. the digitally-represented PSF) is fitted. Collectively, the two steps are referred to as *localization*. Numerous algorithms have been proposed to achieve this, including those based on centroid,[57] Gaussian,[58-61] and radial symmetry techniques.[62, 63] The most prevalent method for fitting is with Gaussian profiles. Table 2 summarizes the most actively used localization methods.

Table 2 : Localization software used in 3D localization microscopy (More info in [64]).

PSF Fitting Method	Compatibility	Available Implementations	Reference
Centroid (Centre-of-Mass)	Single-Plane Astigmatism	QuickPALM	57
Gaussian-Based	Single-Plane Multi-Plane Astigmatism Double Helix	rapi*d*STORM DAOSTORM Multi-Target Tracing µManager FISH-quant	60 58 61 65 59
Radial Symmetry	Single-Plane Multi-Plane		62 63

For PSF engineering-based microscopy methods, emissions are fitted with a prescribed 2D spatial form. In astigmatism techniques, for example, a 2D asymmetric Gaussian profile closely approximates the imposed lateral distortion of the PSF.[23] The lateral (x and y) standard deviations of the profile are afterwards compared to a calibration curve or table to approximate the axial position of the emitting fluorophore.

Direct 3D fitting of emissions may be performed on images acquired using multi-plane techniques (as opposed to indirect 3D fitting in the aforementioned PSF-engineering technique).[59] This can be done with an anisotropic 3D Gaussian profile, with standard deviations corresponding to respective extensions of the PSF in the lateral and axial dimensions. The discussed biplane technique localizes emissions by fitting the recorded projection of the emitter PSF with the experimental 3D PSF using a simplex fitting algorithm.

As a single emitter may give rise to numerous localizations, especially with the use of photoswitchable fluorescent dyes, efforts to deal with localization redundancies is often a necessity. Selection of fluorescent dyes with proper switching properties is especially critical in the case of STORM [66, 67] but it is also important in PALM experiments, notably for single-molecule counting.[68] Generally speaking, however, localization post-treatment is of great importance and is often non-trivial. To this effect, pair-correlation methods, Fourier ring correlation, estimation theory, and nearest neighbour based analysis have been applied to improve notions of localization precision. [69-73] The recent review by Small and Stahlheber provides an overview of algorithmic considerations in single-molecule localization for super-resolution microscopy[74] For calibration and verification of localization accuracy, the use of DNA origami has been proposed for benchmarking.[75]

One of the challenges facing 3D localization microscopy is the density of emitting fluorophores. While it is essential to have sparsely emitting fluorophores in each image frame, reconstructions of the super-resolved image requires a thorough sampling of the entire structure. Hence, tens of thousands of frames are usually acquired in order to form a super-resolved image. The task is more intricate for live-cell super-resolution imaging, as it is essential to record a high number of individual molecule emissions in a time as short as possible. The consequence of high emission densities is that individual PSFs may eventually overlap in a single image. Clearly, distinguishing overlapping fluorophores is an important numerical challenge. Currently, the PSF-dependent fitting technique described in 3D-DAOSTORM presents an approach to overcoming this effect.[76] Although only available in 2D, the Bayesian localization approach discussed in ref [77] also addresses this important challenge.

In practice, there is interplay between the localization density, the image acquisition speed, the localization precision, and the depth of the imaged structure. Principally, the density is critical inasmuch as there is a sufficient number of localized detections to faithfully describe the specimen under observation. This lends itself to considerations on the effective number of detections per emitting molecule, the fluorescence state relative to its dark state lifetime, and overall labeling density,[66] which depends on the type of photoactivatable protein (in the case of PALM) or organic fluorophore (in the case of STORM) that is utilized.

Three-dimensional localizations in an image acquisition sequence can number in the millions, which poses a non-trivial challenge for visual representation. Commercial tools and MATLAB or Python-based scripts can reasonably represent localization along axial projections (slices). However, an interactive viewing of localizations is often more practical. Our recently developed ViSP software,[78] offers a host of features for visualization and quantification, including: a rapid and interactive 3D visualization context, localization-based surface rendering, and measurement of arbitrarily-oriented profiles of localization densities.

Conclusion and Perspectives

Almost ten years after its advent, the benefits of super-resolution imaging in biology are becoming increasingly evident. As a result, there is a need to apply LM in an ever-expanding variety of specimens, which raise several challenges for microscopists and motivates the development of novel optical, chemical and computational techniques. Among the most pressing issues for LM is the need to acquire 3D super-resolution multicolor images in thick samples and in live conditions.

Applications in super-resolution LM have motivated the design and synthesis of new fluorescent proteins and dyes with improved brightness and with emission wavelengths spanning the visible and infrared.[67, 79, 80] This will clearly benefit multicolor super-resolution studies, where several subcellular structures need to be imaged simultaneously. The obvious constraints related to multiple fluorophore selection and their respective spectral separations remain but techniques such as spectral demixing may alleviate this issue.[81, 82]

In many cases, such as the full mapping of the nervous system, one of the goals of the BRAIN project, [83] it would be highly desirable to go beyond cultured cells and acquire super-resolution images in samples such as tissues, brain slices or small organisms. As discussed above, the implementation of light-sheet techniques will surely be instrumental for that purpose. Yet, other tools will be necessary. Indeed, an important issue for LM in thick samples is the potential aberrations that are due to scattering within the biological medium or to the fact that high-NA immersion objectives are used far from the glass coverslip, a regime they are not designed for. In this context, adaptive optics will likely play a key role to optimize the detection of individual fluorophores and maximize the resolution of LM in thick biological specimen.

Since it is clear that the most relevant information on biological processes are usually obtained from dynamic studies and not from fixed samples, it is essential to improve our ability to acquire super-resolution data in living cells. For LM, it means recording the 3D localizations of many individual activated fluorophores in as short a time as possible. Currently, it is possible to acquire live images with a temporal resolution in the range 1-30 s, depending on the sample.[39] Several factors will probably concur to further improve this temporal resolution. First, future improvements in the performance of optoelectronic devices, such as sCMOS cameras,[84] that enable acquisition over a large field of view, at high speeds and with high sensitivity, will play a key role. Next, as noted above, one can anticipate the design of new dyes, either synthetic or genetically-encoded, with enhanced fluorescence properties. Already, progress has been made for fast acquisition of STORM images through optimization of buffer conditions.[67] Finally, a great gain in recording speed will come through the implementation of new computational methods. For instance, algorithms based on compressed sensing concepts allow the analysis of

PALM/STORM 2D images with high density of emitters[85] and their implementation for 3D data will be very beneficial.
In conclusion, super-resolution microscopy is rapidly transforming from a set of cutting-edge techniques into a mature technology. As discussed in this review, LM is already able to provide 3D multicolor images of cultured cells, even in live conditions and it will surely soon be extended to more complex biology samples. As time goes by, one can safely expect super-resolution microscopy to hold true to its original promise and to radically alter our view of biological structures, of their function and of their regulation.

Acknowledgements

We thank Pr. W.E. Moerner, Dr. G. Shtengel and Dr. H. Hess for sharing their 3D super-resolution data. We are grateful to the members of the Transcription Imaging Consortium at HHMI Janelia Farm for their help and discussion. We acknowledge financial support from Paris-Science-Lettres (program ANR-10-IDEX-0001-02 PSL from the French National Research Agency, from France-BioImaging infrastructure supported by the French National Research Agency (ANR-10-INSB-04, « Investments for the future ») and from ANR grant TRIDIMIC.

Notes and References

[a] Laboratoire Physico-Chimie Curie, Institut Curie, CNRS UMR 168, Université Pierre et Marie Curie-Paris 6, 11 rue Pierre et Marie Curie, 75005 Paris, France
[b] Transcription Imaging Consortium, Janelia Farm Research Campus, Howard Hughes Medical Institute, Ashburn, VA 20147, USA
[c] Functional Imaging of Transcription, CNRS UMR8197, Ecole Normale Supérieure, Institut de Biologie de l'ENS, 75005, Paris, France
* : Equal contribution
corresponding author : Maxime Dahan, maxime.dahan@curie.fr

1. B. M. and W. E., *Principles of optics*, 1997.
2. B. Huang, H. Babcock and X. W. Zhuang, *Cell*, 2010, **143**, 1047-1058.
3. C. G. Galbraith and J. A. Galbraith, *J Cell Sci*, 2011, **124**, 1607-1611.
4. R. Fiolka, *J Optics-Uk*, 2013, **15**.
5. L. Schermelleh, R. Heintzmann and H. Leonhardt, *J Cell Biol*, 2010, **190**, 165-175.
6. S. W. Hell, *Nat Methods*, 2009, **6**, 24-32.
7. M. Heilemann, *J Biotechnol*, 2010, **149**, 243-251.
8. J. Lippincott-Schwartz and S. Manley, *Nat Methods*, 2009, **6**, 21-23.
9. R. Heintzmann and G. Ficz, *Method Cell Biol*, 2013, **114**, 525-544.
10. S. W. Hell and J. Wichmann, *Opt Lett*, 1994, **19**, 780-782.
11. M. G. Gustafsson, *Proc Natl Acad Sci U S A*, 2005, **102**, 13081-13086.
12. E. Betzig, G. H. Patterson, R. Sougrat, O. W. Lindwasser, S. Olenych, J. S. Bonifacino, M. W. Davidson, J. Lippincott-Schwartz and H. F. Hess, *Science*, 2006, **313**, 1642-1645.
13. M. J. Rust, M. Bates and X. Zhuang, *Nat Methods*, 2006, **3**, 793-795.
14. S. T. Hess, T. P. Girirajan and M. D. Mason, *Biophys J*, 2006, **91**, 4258-4272.
15. M. Heilemann, S. van de Linde, M. Schuttpelz, R. Kasper, B. Seefeldt, A. Mukherjee, P. Tinnefeld and M. Sauer, *Angew Chem Int Ed Engl*, 2008, **47**, 6172-6176.
16. F. Pinaud, S. Clarke, A. Sittner and M. Dahan, *Nat Methods*, 2010, **7**, 275-285.
17. C. Bräuchle, D. C. Lamb and J. Michaelis, *Single Particle Tracking and Single Molecule Energy Transfer*, Wiley VCH 2010.
18. R. E. Thompson, D. R. Larson and W. W. Webb, *Biophys J*, 2002, **82**, 2775-2783.
19. K. I. Mortensen, L. S. Churchman, J. A. Spudich and H. Flyvbjerg, *Nat Methods*, 2010, **7**, 377-381.
20. M. Speidel, A. Jonas and E. L. Florin, *Opt Lett*, 2003, **28**, 69-71.
21. H. P. Kao and A. S. Verkman, *Biophys J*, 1994, **67**, 1291-1300.
22. B. Huang, W. Wang, M. Bates and X. Zhuang, *Science*, 2008, **319**, 810-813.
23. I. Izeddin, M. El Beheiry, J. Andilla, D. Ciepielewski, X. Darzacq and M. Dahan, *Opt Express*, 2012, **20**, 4957-4967.
24. K. Xu, H. P. Babcock and X. Zhuang, *Nat Methods*, 2012, **9**, 185-188.
25. C. G. Specht, I. Izeddin, P. C. Rodriguez, M. El Beheiry, P. Rostaing, X. Darzacq, M. Dahan and A. Triller, *Neuron*, 2013, **79**, 308-321.
26. H. Aoki, K. Mori and S. Ito, *Soft Matter*, 2012, **8**, 4390-4395.
27. S. R. Pavani, M. A. Thompson, J. S. Biteen, S. J. Lord, N. Liu, R. J. Twieg, R. Piestun and W. E. Moerner, *Proc Natl Acad Sci U S A*, 2009, **106**, 2995-2999.
28. A. Gahlmann, J. L. Ptacin, G. Grover, S. Quirin, A. R. von Diezmann, M. K. Lee, M. P. Backlund, L. Shapiro, R. Piestun and W. E. Moerner, *Nano Lett*, 2013, **13**, 987-993.
29. S. Jia, J. C. Vaughan and X. Zhuang, *Nature Photonics*, 2014, **8**, 302-306.
30. M. J. Mlodzianoski, M. F. Juette, G. L. Beane and J. Bewersdorf, *Opt Express*, 2009, **17**, 8264-8277.
31. M. F. Juette, T. J. Gould, M. D. Lessard, M. J. Mlodzianoski, B. S. Nagpure, B. T. Bennett, S. T. Hess and J. Bewersdorf, *Nat Methods*, 2008, **5**, 527-529.
32. B. Hajj and al., *Submitted*.
33. P. Kanchanawong, G. Shtengel, A. M. Pasapera, E. B. Ramko, M. W. Davidson, H. F. Hess and C. M. Waterman, *Nature*, 2010, **468**, 580-584.
34. B. G. Kopek, G. Shtengel, C. S. Xu, D. A. Clayton and H. F. Hess, *Proc Natl Acad Sci U S A*, 2012, **109**, 6136-6141.
35. G. Shtengel, J. A. Galbraith, C. G. Galbraith, J. Lippincott-Schwartz, J. M. Gillette, S. Manley, R. Sougrat, C. M. Waterman, P. Kanchanawong, M. W. Davidson, R. D. Fetter and H. F. Hess, *Proc Natl Acad Sci U S A*, 2009, **106**, 3125-3130.
36. K. A. Sochacki, B. T. Larson, D. C. Sengupta, M. P. Daniels, G. Shtengel, H. F. Hess and J. W. Taraska, *Nat Commun*, 2012, **3**, 1154.

37. D. Aquino, A. Schonle, C. Geisler, C. V. Middendorff, C. A. Wurm, Y. Okamura, T. Lang, S. W. Hell and A. Egner, *Nat Methods*, 2011, **8**, 353-359.
38. J. Tang, J. Akerboom, A. Vaziri, L. L. Looger and C. V. Shank, *Proc Natl Acad Sci U S A*, 2010, **107**, 10068-10073.
39. F. Cella Zanacchi, Z. Lavagnino, M. Perrone Donnorso, A. Del Bue, L. Furia, M. Faretta and A. Diaspro, *Nat Methods*, 2011, **8**, 1047-1049.
40. A. G. York, A. Ghitani, A. Vaziri, M. W. Davidson and H. Shroff, *Nat Methods*, 2011, **8**, 327-333.
41. A. Vaziri, J. Tang, H. Shroff and C. V. Shank, *Proc Natl Acad Sci U S A*, 2008, **105**, 20221-20226.
42. G. Grover, S. Quirin, C. Fiedler and R. Piestun, *Biomed Opt Express*, 2011, **2**, 3010-3020.
43. M. D. Lew, S. F. Lee, M. Badieirostami and W. E. Moerner, *Opt Lett*, 2011, **36**, 202-204.
44. S. Ram, P. Prabhat, J. Chao, E. S. Ward and R. J. Ober, *Biophys J*, 2008, **95**, 6025-6043.
45. P. Prabhat, S. Ram, E. S. Ward and R. J. Ober, *IEEE Trans Nanobioscience*, 2004, **3**, 237-242.
46. M. J. Mlodzianoski, J. M. Schreiner, S. P. Callahan, K. Smolkova, A. Dlaskova, J. Santorova, P. Jezek and J. Bewersdorf, *Opt Express*, 2011, **19**, 15009-15019.
47. J. Ries, C. Kaplan, E. Platonova, H. Eghlidi and H. Ewers, *Nat Methods*, 2012, **9**, 582-584.
48. J. Chao, S. Ram, E. S. Ward and R. J. Ober, *Opt Express*, 2009, **17**, 24377.
49. J. Chao, S. Ram, A. V. Abraham, E. S. Ward and R. J. Ober, Biomedical Optics (BiOS) 2008, 2008.
50. M. F. Juette and J. Bewersdorf, *Nano Lett*, 2010, **10**, 4657-4663.
51. S. Ram, D. Kim, R. J. Ober and E. S. Ward, *Biophys J*, 2012, **103**, 1594-1603.
52. S. Ram, P. Prabhat, E. S. Ward and R. J. Ober, *Opt Express*, 2009, **17**, 6881-6898.
53. S. Abrahamsson, J. Chen, B. Hajj, S. Stallinga, A. Y. Katsov, J. Wisniewski, G. Mizuguchi, P. Soule, F. Mueller, C. Dugast Darzacq, X. Darzacq, C. Wu, C. I. Bargmann, D. A. Agard, M. Dahan and M. G. Gustafsson, *Nat Methods*, 2013, **10**, 60-63.
54. J. Wisniewski, B. Hajj, J. Chen, G. Mizuguchi, H. Xiao, W. Wei, M. Dahan and C. Wu, *Submitted*, 2014.
55. C. von Middendorff, A. Egner, C. Geisler, S. W. Hell and A. Schonle, *Opt Express*, 2008, **16**, 20774-20788.
56. Y. Sun, J. D. McKenna, J. M. Murray, E. M. Ostap and Y. E. Goldman, *Nano Lett*, 2009, **9**, 2676-2682.
57. R. Henriques, M. Lelek, E. F. Fornasiero, F. Valtorta, C. Zimmer and M. M. Mhlanga, *Nat Methods*, 2010, **7**, 339-340.
58. S. J. Holden, S. Uphoff and A. N. Kapanidis, *Nat Methods*, 2011, **8**, 279-280.
59. F. Mueller, A. Senecal, K. Tantale, H. Marie-Nelly, N. Ly, O. Collin, E. Basyuk, E. Bertrand, X. Darzacq and C. Zimmer, *Nat Methods*, 2013, **10**, 277-278.
60. S. Wolter, A. Loschberger, T. Holm, S. Aufmkolk, M. C. Dabauvalle, S. van de Linde and M. Sauer, *Nat Methods*, 2012, **9**, 1040-1041.
61. A. Serge, N. Bertaux, H. Rigneault and D. Marguet, *Nat Methods*, 2008, **5**, 687-694.
62. R. Parthasarathy, *Nat Methods*, 2012, **9**, 724-726.
63. S. L. Liu, J. Li, Z. L. Zhang, Z. G. Wang, Z. Q. Tian, G. P. Wang and D. W. Pang, *Sci Rep*, 2013, **3**, 2462.
64. , bigwww.epfl.ch/smlm/software/index.html.
65. A. Edelstein, N. Amodaj, K. Hoover, R. Vale and N. Stuurman, *Curr Protoc Mol Biol*, 2010, **Chapter 14**, Unit14 20.
66. S. van de Linde, S. Wolter, M. Heilemann and M. Sauer, *J Biotechnol*, 2010, **149**, 260-266.
67. G. T. Dempsey, J. C. Vaughan, K. H. Chen, M. Bates and X. Zhuang, *Nat Methods*, 2011, **8**, 1027-1036.
68. S. H. Lee, J. Y. Shin, A. Lee and C. Bustamante, *Proc Natl Acad Sci U S A*, 2012, **109**, 17436-17441.
69. N. Banterle, K. H. Bui, E. A. Lemke and M. Beck, *J Struct Biol*, 2013, **183**, 363-367.
70. P. Sengupta, T. Jovanovic-Talisman, D. Skoko, M. Renz, S. L. Veatch and J. Lippincott-Schwartz, *Nat Methods*, 2011, **8**, 969-975.
71. R. P. Nieuwenhuizen, K. A. Lidke, M. Bates, D. L. Puig, D. Grunwald, S. Stallinga and B. Rieger, *Nat Methods*, 2013, **10**, 557-562.
72. J. E. Fitzgerald, J. Lu and M. J. Schnitzer, *Phys Rev Lett*, 2012, **109**, 048102.
73. U. Endesfelder, S. Malkusch, F. Fricke and M. Heilemann, *Histochem Cell Biol*, 2014.
74. A. Small and S. Stahlheber, *Nat Methods*, 2014, **11**, 267-279.
75. J. J. Schmied, C. Forthmann, E. Pibiri, B. Lalkens, P. Nickels, T. Liedl and P. Tinnefeld, *Nano Lett*, 2013, **13**, 781-785.
76. H. Babcock, Y. M. Sigal and X. Zhuang, *Optical Nanoscopy*, 2012, **1**.
77. S. Cox, E. Rosten, J. Monypenny, T. Jovanovic-Talisman, D. T. Burnette, J. Lippincott-Schwartz, G. E. Jones and R. Heintzmann, *Nat Methods*, 2012, **9**, 195-200.
78. M. El Beheiry and M. Dahan, *Nat Methods*, 2013, **10**, 689-690.
79. S. A. McKinney, C. S. Murphy, K. L. Hazelwood, M. W. Davidson and L. L. Looger, *Nat Methods*, 2009, **6**, 131-133.
80. G. Lukinavicius, K. Umezawa, N. Olivier, A. Honigmann, G. Yang, T. Plass, V. Mueller, L. Reymond, I. R. Correa, Jr., Z. G. Luo, C. Schultz, E. A. Lemke, P. Heppenstall, C. Eggeling, S. Manley and K. Johnsson, *Nat Chem*, 2013, **5**, 132-139.
81. D. Baddeley, D. Crossman, S. Rossberger, J. E. Cheyne, J. M. Montgomery, I. D. Jayasinghe, C. Cremer, M. B. Cannell and C. Soeller, *PLoS One*, 2011, **6**, e20645.
82. A. Lampe, V. Haucke, S. J. Sigrist, M. Heilemann and J. Schmoranzer, *Biol Cell*, 2012, **104**, 229-237.
83. E. R. Kandel, H. Markram, P. M. Matthews, R. Yuste and C. Koch, *Nat Rev Neurosci*, 2013, **14**, 659-664.
84. F. Huang, T. M. Hartwich, F. E. Rivera-Molina, Y. Lin, W. C. Duim, J. J. Long, P. D. Uchil, J. R. Myers, M. A. Baird, W. Mothes, M. W. Davidson, D. Toomre and J. Bewersdorf, *Nat Methods*, 2013, **10**, 653-658.
85. L. Zhu, W. Zhang, D. Elnatan and B. Huang, *Nat Methods*, 2012, **9**, 721-723.